Research Square

Preprints are preliminary reports that have not undergone peer review.
They should not be considered conclusive, used to inform clinical practice,
or referenced by the media as validated information.

High Entropy Effect Induced In-situ Surface Hydroxylation for Robust Electro-Assisted Uranium Mineralization from Real Nuclear Wastewater

Wenkun Zhu
zhuwenkun@swust.edu.cn
Southwest University of Science and Technology https://orcid.org/0000-0002-4116-6213
Tao Chen
Southwest University of Science and Technology
Hailin Wu
Southwest University of Science and Technology
Xiaofang Feng
Southwest University of Science and Technology
Xiaochuan Deng
Southwest University of Science and Technology
Xun Yang
Southwest University of Science and Technology
Wenjie Sun
Southwest University of Science and Technology
Xue Jiang
Southwest University of Science and Technology
Liwen Zhou
Southwest University of Science and Technology
Zicheng Yao
Southwest University of Science and Technology

Article

Keywords: in-situ hydroxylation, high-entropy oxides, electro-assisted, uranium extraction, real nuclear wastewater

Posted Date: February 27th, 2026

DOI: https://doi.org/10.21203/rs.3.rs-7778222/v1

License: This work is licensed under a Creative Commons Attribution 4.0 International License. Read Full License

Additional Declarations: There is **NO** Competing Interest.

Version of Record: A version of this preprint was published at Nature Communications on September 1st, 2026. See the published version at https://doi.org/10.1038/s41467-026-76781-0.

Abstract

Exploring highly active and cost-efficient electrocatalysts with in-situ regeneration of coordination sites is crucial for the large-scale application of electro-assisted uranium extraction technology, which can effectively solve the problem of limited coordination sites for traditional catalysts. Herein, we tailor the charge distribution of La(CrFeCoNiCu)O_3 via high-entropy effect to induce in-situ surface hydroxylation, thereby enabling robust uranium recovery from fluoride-containing uranium wastewater. The as-prepared La(CrFeCoNiCu)O_3 exhibits exceptional uranium removal performance, achieving a 97.8% removal rate in fluoride-containing uranium wastewater and still maintaining over 91.3% efficiency with real uranium wastewater. Relying on in-situ ATR-SEIRAS and quasi-in-situ XPS, we confirm that Cu sites serve as hydroxylation active sites, enabling precise capture of fluoro-uranium complexes, followed by uranium mineralization via electron reduction-free radical reoxidation pathway. In addition, large-scale application verification of real nuclear wastewater is conducted on the self-designed flow electrolysis device, confirming its cost advantage.

1. Introduction

As a key foundational resource for nuclear energy, uranium resources, known as the granary and cornerstone of nuclear power, will be depleted in less than a century[1]. The shortage of uranium resources has forced scientists to shift their focus from traditional uranium resources to unconventional uranium resources[2]. Fluorine-containing uranium wastewater, as a typical unconventional uranium resource, is mainly generated from the hydrolysis of uranium fluoride (UF_6) during fuel production[3]. In fluoride-containing uranium wastewater, the uranium concentration is generally greater than 100 mg L^{-1}, and the coexisting F^- concentration can reach up to 30 g L^{-1}.[4] The competitive coordination between fluoride and uranium can form complexes such as UO_2F^+, UO_2F_2 (aq), $UO_2F_3^-$, etc., making traditional treatment processes particularly difficult for treating fluoride-containing uranium wastewater[5]. As an emerging technology, electro-assisted uranium extraction has attracted ever-increasing attention[6].

So far, various electrode materials such as metal sulfides[7], metal oxides[8], covalent organic frameworks[9], metal nitrogen carbides[10] have been developed for extracting uranium from various nuclear wastewater, seawater, and mineralized wastewater. Among electrode materials, metal oxides stand as promising candidates due to their tunable conductivity, exceptional stability, and low cost[11]. However, the limited coordination sites in metal oxides greatly limit their continuous selective coordination reduction of uranium species from aqueous solutions. The emergence of high-entropy oxide (HEO) provides an opportunity to solve the problem of limited coordination sites. High-entropy oxides are prone to trigger surface dynamic reconstruction during electrochemical processes and generate highly active coordination sites in-situ via the synergistic effect of multiple elements (cocktail effect) and lattice stabilization driven by entropy increase[12]. This processes do not require post-synthesis modification and spontaneously coordinate the electronic structures and active sites distribution of the electrode, thereby achieving intrinsic performance optimization[13]. Notably, the perovskite-type (ABO_3) oxides, as one of the star materials in electrocatalysis, possess a highly tunable crystal structure that enables the integration of diverse elements at the B-site to form high-entropy configurations[14]. Therefore, the development of ABO_3-type high-entropy oxides electrode materials suitable for electro-assisted uranium extraction is expected to achieve efficient uranium extraction from fluoride-containing uranium wastewater.

Herein, we reported an in-situ surface hydroxylation strategy induced by high entropy effect in high-entropy oxides for the recovery of uranium from fluoride-containing uranium wastewater. Firstly, density functional theory (DFT) calculations were used to predict the in-situ hydroxylation activity of transition metals in high entropy oxides, following the trend of Cu > Fe>Co > Ni>Cr, in which Cu sites possess the lowest M-OH formation energy due to their optimized local electron density. Based on the theory prediction, a modified sol-gel method strategy was proposed to fabricate a La(CrFeCoNiCu)O_3 high-entropy oxide. The as-constructed La(CrFeCoNiCu)O_3 high-entropy oxide demonstrate remarkable uranium extraction ability (> 97.8%) in fluoride-containing uranium wastewater. By virtue of in-situ ATR-SEIRAS and quasi-in-situ XPS, along with DFT calculations, we have proven the feasibility of the in-situ hydroxylation strategy and confirmed that Cu sites serve as hydroxylation active sites, consistent with previous predictions. Theoretical calculations demonstrate that the superior performance of La(CrFeCoNiCu)O_3 originates from electron accumulation at Cu sites induced by the high-entropy effect, which consequently promotes in-situ hydroxylation during the reaction and enhances uranyl capture capability. This study provides a new insight into the in-situ design of metal oxides surface coordination sites for the electro-assisted recovery of uranium from fluoride-containing wastewater.

2. Experimental

2.1. Materials and Chemicals

All chemicals were used as received without further purification. Lanthanum nitrate hexahydrate ($La(NO_3)_3{\cdot}6H_2O$), Chromium (III) nitrate nonahydrate ($Cr(NO_3)_3{\cdot}9H_2O$), Iron (III) nitrate nonahydrate ($Fe(NO_3)_3{\cdot}9H_2O$), Cobalt nitrate hexahydrate ($Co(NO_3)_2{\cdot}6H_2O$), Nickel nitrate

hexahydrate ($Ni(NO_3)_2·6H_2O$), Copper nitrate trihydrate ($Cu(NO_3)_2·3H_2O$), Ammonium citrate ($C_6H_{17}N_3O_7$), and Ethylene glycol ($C_2H_6O_2$) were purchased from Aladdin Chemistry Co., Ltd. (Shanghai, China). Uranyl Nitrate Hexahydrate ($UO_2(NO_3)_2·6H_2O$), Arsenazo Ⅲ ($C_{16}H_{10}AsN_2Na_3O_{11}S_2$), and Nafion (5 wt%) solution were purchased from Macklin Biochemical Technology Co., Ltd. (Shanghai, China). Deionized water (18.25 MΩ) was used in all experiments.

2.2. Synthesis of $La(CrFeCoNiCu)O_3$, $La(CrCoNi)O_3$ and $LaCrO_3$

The synthesis method of $La(CrFeCoNiCu)O_3$ is similar to the reported research. Specifically, 8 mmol of $La(NO_3)_3·6H_2O$, 1.6 mmol $Cr(NO_3)_3·9H_2O$, 1.6mmol $Fe(NO_3)_3·9H_2O$, 1.6 mmol $Co(NO_3)_2·6H_2O$, 1.6 mmol $Ni(NO_3)_2·6H_2O$, 1.6 mmol $Cu(NO_3)_2·3H_2O$ and 37.5 mmol of Ammonium citrate (AC) were dissolved in 25 mL deionized water. Then, 24 mL Ethylene glycol (EG) was added to the above solution under vigorous stirring to form a homogeneous solution. The resulting homogeneous solution was heated at 120°C for approximately 10 h to obtain a wet gel. To obtain the final product $La(CrFeCoNiCu)O_3$, the wet gel was heated to 600°C at 15°C min^{-1} and calcined for 2 h under air atmosphere. $La(CrCoNi)O_3$ and $LaCrO_3$ were synthesized using protocols analogous to $La(CrFeCoNiCu)O_3$ with solely altered transition metal nitrate precursors.

2.3. Electrochemical measurements

Unless otherwise specified, all electrochemical tests were conducted using a standard three-electrode system on CHI 660E electrochemical workstation. Ag/AgCl electrode and platinum electrode were using as reference electrode and counter electrode respectively. The working electrodes were prepared by mixing 5 mg of materials, 20 mL of Nafion (5 wt%) solution, and 2 mL of ethanol under ultrasound to form a homogeneous ink. Then, the as-prepared ink was evenly loaded onto 1×2 cm carbon paper and dried at 80°C to evaporate the solvent. Uranium extraction experiments were conducted in 50 mL electrolyte containing 100 ppm U and 30 g L^{-1} fluoride ions. For real nuclear wastewater experiments, working electrodes were prepared similarly to the aforementioned procedure, with 15 mg or 400 mg catalyst uniformly loaded onto 2×2 or 5×5 cm carbon paper, respectively. More details can be obtained in the Supporting Information.

2.4. Theoretical calculations

The calculations were carried out within the density functional theory (DFT) framework implanted in Vienna ab initio Simulation Package (VASP6.3.2)[15]. The interaction between ions and electrons was described in the Projector Augmented Wave (PAW) Method[16]. The electron exchange and correlation energy were described using the generalized gradient approximation-based Perdew-Burke-Erzenhorf (PBE) functional[17]. The semi-empirical London dispersion corrections of Grimme and colleagues (DFT-D3) were conducted to calculate the interactions between absorbers and slabs[18].

2.5. Characterization

The morphology and energy dispersive X-ray spectroscopy (EDS) images were displayed on a ZEISS Sigma 300 scanning electron microscope (SEM). Transmission electron microscopy images and high-resolution transmission electron microscopy images were obtained on a JEM-F200 transmission electron microscope (TEM). The crystal structure data was tested on a PANalytic Empyrean X-ray diffractometer (XRD) equipped with a Cu kα resource. The chemical valence states of the elements were analyzed using X-ray photoelectron spectroscopy (XPS) and tested on a Thermo ESCELAB 250XI. The uranium concentration was obtained by inductively coupled plasma mass spectrometry (ICP-MS Agilent 7700) and UV-vis transmittance spectra (PE Lambda 650 UV vis NIR spectrophotometer). Surface area and pore size distribution (BET) were measured using a Micromeritics TriStar II 3020/3Flex analyzer. Fourier Transform Infrared Spectroscopy (FT-IR) and in-situ attenuated total reflectance-surface enhanced infrared absorption spectroscopy (ATR-SEIRAS) measurements were both conducted on INSA OPTICS FOLI20-R-T. X-ray absorption fine structure (XAFS) spectroscopy was carried out using the RapidXAFS 2M (Anhui Absorption Spectroscopy Analysis Instrument Co., Ltd.) by transmission(or fluorescence) mode at 20 kV and 20 mA, and the Si (6612) spherically bent crystal analyzer with a radius of curvature of 500 mm was used for U.

3. Results and discussion

3.1. Materials Design Concept: In-situ Hydroxylation of High-entropy Oxides

For ABO_3 crystal structure, the B-site exhibits extensive elemental compatibility and valence flexibility, while the periodic arrangement of A-site elements can form a stable framework structure with excellent inclusiveness, allowing multiple different B-site elements to be flexibly incorporated[19]. This robust framework structure serves as a natural platform for building high-entropy oxides, providing natural architectural advantages for materials design. Herein, we take the typical rare-earth element La as the framework and incorporate common, valence variable, and electrocatalytically active 3*d* transition metals (Cr, Fe, Co, Ni, Cu) into the skeleton (Fig. 1a). By increasing the types of B-site elements, the *d*-orbital interactions of different metals may lead to a more diverse local electronic environment on the surface of high-entropy

oxides[20]. Thus, for high-entropy oxides, B-site metals with variable valence states are easily reduced to form hydroxylation active sites (M-OH) in-situ under operating conditions, thereby enhancing the selective capture ability of uranium (Fig. 1b)[21].

To further verify the validity of the above hypothesis, we conducted density functional theory (DFT) calculations by utilizing La(CrFeCoNiCu)O_3 slab and $LaCrO_3$ slab as structural models (Supplementary Fig. 1). The formation energy of M-OH from the B-site metals of La(CrFeCoNiCu)O_3 slab and $LaCrO_3$ slab was used to evaluate the difficulty of hydroxylation of ABO_3 oxides. As expected, the formation energy of M-OH for Cr-site of $LaCrO_3$ slab is 2.52 eV, far higher than La(CrFeCoNiCu)O_3. For La(CrFeCoNiCu)O_3, the formation energy of M-OH for Cu site is -0.892 eV, far lower than the others metal (Fe, Co, Ni, Cr) (Fig. 1c and 1d). Therefore, theoretically, we have reason to conclude that the surface Cu sites in La(CrFeCoNiCu)O_3 are most likely to undergo reconstruction and form M-OH, while $LaCrO_3$ hardly forms hydroxyl groups in-situ. Meanwhile, the electron localization function (ELF) mappings were further employed to evaluate the electron distributions of $LaCrO_3$, La(CrFeCoNiCu)O_3, and reconstructioned La(CrFeCoNiCu)O_3-OH (representing hydroxylation), where the colors indicate the localization states of electrons (Fig. 1d and supplementary Fig. 2). Compared with $LaCrO_3$ and pristine La(CrFeCoNiCu)O_3, more electrons localized near the hydroxyl groups in La(CrFeCoNiCu)O_3-OH, which further indicates that M-OH is most likely to serve as uranyl confinement coordination sites based on the soft hard acid-base theory[22].

Taking UO_2^{2+} and UO_2F^+ as representatives of uranium species in fluoride-containing uranium wastewater, their adsorption energies on $LaCrO_3$ and La(CrFeCoNiCu)O_3-OH were calculated (Supplementary Figs. 3 and 4). As expected, the adsorption energies of UO_2^{2+} and UO_2F^+ for La(CrFeCoNiCu)O_3-OH are − 3.69 eV and − 2.67 eV, much lower than those on $LaCrO_3$ (-2.81 eV and − 2.40 eV). The above results further confirmed that the M-OH sites of reconstructed La(CrFeCoNiCu)O_3-OH is the most likely coordination sites for selective coordination of uranyl. In addition, the electron transfer between uranium species (UO_2^{2+} and UO_2F^+) and the substrates ($LaCrO_3$ and La(CrFeCoNiCu)O_3-OH) was further investigated through differential charge density (DCD), Bader charge analysis, and ELF mapping. As shown in Fig. 1e and Supplementary Fig. 5, compared with $LaCrO_3$, the charge transfer between UO_2F^+ and La(CrFeCoNiCu)O_3-OH is more pronounced, accompanied by a higher degree of electron localization at the adsorption interface, further illustrating the anchoring effect of M-OH on uranium species.

This assertion is also strongly supported by the crystal orbital Hamiltonian population (COHP) curves. The negative iCOHP (integrated crystal orbital Hamiltonian population) value corresponds to the bonding property[23]. Compared to $LaCrO_3$ (− 5.449 eV), the U-O bond value in La(CrFeCoNiCu)O_3-OH is lower (-5.571 eV), implying the formation of stronger chemical bonds between uranium and La(CrFeCoNiCu)O_3-OH (Fig. 1f and 1g). Based on the aforementioned findings, we have reason to believe that La(CrFeCoNiCu)O_3 can undergo in-situ hydroxylation-mediated structural reconstruction under operational conditions, thereby significantly improving its selective coordination and reduction performance for uranium species.

3.2. Precise Synthesis and Characterization of La(CrFeCoNiCu)O_3 High-Entropy Oxides

Inspired by DFT calculations, we develop a modified sol-gel method for synthesizing La(CrFeCoNiCu)O_3 high-entropy oxides[24]. And La(CrCoNi)O_3 as well as $LaCrO_3$ were obtained by varying the molar ratios and types of nitrate precursors (Fig. 2a and Supplementary Fig. 6). As shown in Fig. 2b and Supplementary Fig. 7, the Scanning electron microscopy (SEM) images of La(CrFeCoNiCu)O_3, La(CrCoNi)O_3, and $LaCrO_3$ all exhibited unique porous coral-like structures. Notably, the Brunauer-Emmett-Teller (BET) specific surface area of La(CrFeCoNiCu)O_3 (21.66 $m^2\ g^{-1}$) is significantly higher than those of La(CrCoNi)O_3 (17.01 $m^2\ g^{-1}$) and $LaCrO_3$ (14.98 $m^2\ g^{-1}$), which may be attributed to the slow diffusion effect induced by multi cation introduction[25]. (Supplementary Fig. 8). Inductively coupled plasma mass spectrometry (ICP-MS) confirmed that the elemental composition of La(CrFeCoNiCu)O_3 matched the intended stoichiometry (Fig. 2b inset). The calculated configurational entropy (ΔS_{conf}) of La(CrFeCoNiCu)O_3 was ca. 1.807 R (> 1.5 R), met the criterion for high-entropy oxides[26].

Energy-dispersive X-ray spectroscopy (EDS) mapping further verified the homogeneous distribution of all constituent elements (Fig. 2c and Supplementary Fig. 9, 10). The crystal structures of La(CrFeCoNiCu)O_3, La(CrCoNi)O_3, and $LaCrO_3$ were examined by X-ray diffraction (XRD). The diffraction peaks at 2θ values of 22.93°, 32.55°, 40.12°, 46.88°, and 58.14° are assigned to the (002), (112), (202), (004), and (204) planes, respectively (Fig. 2d), which are characteristic of the orthorhombic perovskite Pbnm space group (JCPDS: PDF#24-1016)[27]. The absence of impurity peaks confirmed the phase-pure perovskite structure of La(CrFeCoNiCu)O_3. Rietveld refinement showed excellent agreement between the simulated and experimental XRD patterns, revealing randomly occupying of the B-site by Cr, Fe, Co, Ni, and Cu at an equal ratio of 1/5 (Fig. 2e and Table 1, 2), further validating its high-entropy nature[28]. The Fourier-transform infrared (FT-IR) spectrum of La(CrFeCoNiCu)O_3 displayed an absorption band at 610 cm^{-1}, attributed to the Cr–O stretching vibration, similar to that of $LaCrO_3$ (Supplementary Fig. 11)[29]. The

selected-area electron diffraction (SAED) patterns revealed diffraction rings consistent with those of $LaCrO_3$ (Fig. 2f inset), reinforcing the single-phase perovskite structure. Meanwhile, the high-resolution transmission electron microscopy (HRTEM) image of La(CrFeCoNiCu)O_3 showed distinct significant interplanar spacings of 0.3814 and 0.2749 nm, assigned to the (002) and (112) planes of $LaCrO_3$ (Supplementary Fig. 12), respectively[30]. Figure 2f and 2g present high-angle annular dark-field scanning transmission electron microscopy (HAADF-STEM) images of La(CrFeCoNiCu)O_3, including an enlarged area. Owing to its higher atomic number (Z), La displayed brighter contrast relative to the transition metals (e.g., Cr, Fe, Co, Ni, Cu)[31]. HAADF-STEM images under polarized mode further revealed the spatial distributions of La and the transition metals (Fig. 2h). In addition, X-ray photoelectron spectroscopy (XPS) measurement were carried out to investigate the chemical valences of La(CrFeCoNiCu)O_3, La(CrCoNi)O_3 and $LaCrO_3$ (Supplementary Fig. 13). In the La(CrFeCoNiCu)O_3 spectra, the La 3*d* peaks shifted toward lower binding energies, while Cr 2*p* peaks shifted to higher binding energies. Concurrently, the Cr^{6+}/Cr^{3+} and Co^{3+}/Co^{2+} ratios increased accordingly, indicating elevated oxidation states of Cr and Co[32]. These results suggested the synergistic electronic interactions among constituent elements in the multicomponent La(CrFeCoNiCu)O_3. Collectively, these results confirmed the successful synthesis of phase-pure orthorhombic perovskite La(CrFeCoNiCu)O_3.

3.3. Electrochemical uranium extraction

To verify that in-situ hydroxylation of La(CrFeCoNiCu)O_3 during electrochemical processes can enhance uranium capture capability, experiments were conducted in simulated nuclear wastewater containing 100 mg L^{-1} U(VI) and 30 g L^{-1} F^- (Fig. 3a). Linear sweep voltammetry (LSV) tests revealed that La(CrFeCoNiCu)O_3 exhibited a lower uranium reduction potential compared with $LaCrO_3$ and La(CrCoNi)O_3, while no reduction peaks were observed on pure carbon paper (Fig. 3b). This indicates that uranyl ions (UO_2^{2+}) are more readily reduced on La(CrFeCoNiCu)O_3. The uranium extraction performance was further evaluated under applied voltage of 0 V (no applied voltage), -1 V, and − 1.3 V. As shown in Supplementary Fig. 14, all three materials exhibited uniformly low extraction efficiencies (ca. 16%) at 0 V, where only physicochemical adsorption dominated. At − 1 V and − 1.3 V, their extraction efficiencies remained comparable (ca. 50%), showing no significant differences. Surprisingly, when the voltage was increased to -1.7 V, the extraction efficiency of La(CrFeCoNiCu)O_3 exceeded 90% in 360 min, significantly higher than those of La(CrCoNi)O_3 and $LaCrO_3$ (Fig. 3c). With the reaction time prolong, the uranium extraction efficiency can exceed 98%. The reaction kinetic constant (*k*) of La(CrFeCoNiCu)O_3 was calculated to be 0.00675 min^{-1}, which is 1.93-fold and 3.90-fold higher than those of La(CrCoNi)O_3 (0.00349 min^{-1}) and $LaCrO_3$(0.00173 min^{-1}), respectively (Fig. 3d). This discrepancy may be due to the insufficient energy provided by the external electric field at low voltages (≤ -1.3 V) to trigger the surface hydroxylation of La(CrFeCoNiCu)O_3, resulting in no significant differences in uranium extraction efficiency[33]. In contrast, at high voltage (-1.7 V), the surface hydroxylation is activated, inducing the formation of M-O-H active structures, which ultimately leads to differentiation in uranium extraction performance.

At an applied of -1.7 V, the influences of key operational parameters on the uranium extraction performance of La(CrFeCoNiCu)O_3 were further probed. Initially, the uranium extraction efficiency of La(CrFeCoNiCu)O_3 was evaluated across initial U(VI) concentration ranging from 50 to 250 mg L^{-1}. As shown in Fig. 3e, La(CrFeCoNiCu)O_3 maintained favorable uranium extraction performance across a wide range of initial uranium concentrations. Specifically, even when the initial uranium concentration reached 250 mg L^{-1}, the extraction efficiency remained above 92%, with the uranium adsorption capacity reached 2385.8 mg g^{-1}. Given that fluoride-containing uranium wastewater readily form uranyl-fluoride complexes that impede extraction, uranium extraction performance was further assessed under varying F^- concentrations (5–30 g L^{-1}). Remarkably, uranium extraction efficiency remained above 93% across this range (Supplementary Fig. 15). The pH variations are recognized as a critical factor influencing uranium extraction efficiency, with pH changes often inducing structural transitions in uranyl-fluoride complexes and thereby affecting extraction performance. Thus, the uranium extraction efficiency of La(CrFeCoNiCu)O_3 was evaluated across a pH range of 5 to 10. Results showed that extraction efficiency remained nearly unaffected within this pH window (Supplementary Fig. 16). In addition, uranium-containing wastewater typically contains various coexisting ions, which may reduce uranium extraction efficiency. The effects of typical coexisting ions (SO_4^{2-}, NO_3^-, NH_4^+, CO_3^{2-}, Cl^-, $C_2O_4^{2-}$) in fluoride-rich uranium wastewater on extraction efficiency were examined. While these ions caused a slight reduction, uranium extraction efficiency consistently exceeded 85%, demonstrating robust anti-interference capability (Fig. 3f). In addition, the extraction efficiency exhibited no significant decline and remained above 92% after six cycles of reuse (Fig. 3g). Post-extraction characterization revealed uniform lamellar uranium deposition on the materials surface via SEM/EDS (Fig. 3h). The XRD pattern and XPS spectrum confirmed that the extracted uranium product is a mixed-valent $K_3UO_2F_5$ (JCPDS:01-078-2148), which can be attributed to the reoxidation of some low valance uranium species by relevant free radicals generated during the reaction process (such as $\cdot O_2^-$, ·OH, and $\cdot CO_3^-$) (Supplementary Figs. 17–19). Additionally, the characteristic peaks of the collected uranium products showed close alignment with standard $K_3UO_2F_5$ in infrared spectra, further verifying the compound identity (Supplementary Fig. 20). Compared with the reported materials, La(CrFeCoNiCu)O_3 also presented remarkable uranium extraction efficiency under high fluoride conditions (Fig. 3i)[34–40]. These findings emphasized the application potential of La(CrFeCoNiCu)O_3 for uranium recovery from high-fluoride uranium-containing wastewater via electro-assisted methods.

3.4. Mechanistic Study of reconstruction-Mediated M-O-H Active Sites

The excellent performance of La(CrFeCoNiCu)O_3 in electro-assisted uranium extraction experiments prompted us to investigate its origin. To monitor the in-situ surface hydroxylation and intermediate uranium species desorption processes of La(CrFeCoNiCu)O_3 under working conditions, we employed in-situ attenuated total reflection surface-enhanced infrared absorption spectroscopy (ATR-SEIRAS) (Fig. 4a and 4b). As the reaction progresses, the intensity of the characteristic absorption peak near 1011 cm^{-1}, assigned to the bending vibration (δ_{M-OH}) of surface hydroxyl groups on the perovskite, gradually increased and exhibited a certain degree of blueshift over time[41]. This indicates the gradual hydroxylation on the surface of La(CrFeCoNiCu)O_3, providing a continuous source of active sites for subsequent uranium selective capture. Similar phenomena have also been observed in both uranium-only and fluoride-only solutions (Supplementary Figs. 21 and 22), further confirming the universality of in-situ hydroxylation of La(CrFeCoNiCu)O_3 surfaces. Notably, concurrent with the rising intensity of the M–OH peak, new absorption peaks gradually emerge at 710 cm^{-1}, 774 cm^{-1}, and 820 cm^{-1}, assigned to the symmetric U = O stretching vibration, U-O stretching vibration, and U = O out-of-plane bending vibration, respectively[42–44]. In contrast, for $LaCrO_3$, no changes in the M-OH characteristic peaks were observed with the extension of reaction time in the aforementioned solution media (Supplementary Fig. 23). In addition, the O 1s XPS spectrum can also confirm the in-situ hydroxylation of La(CrFeCoNiCu)O_3 surface (Supplementary Fig. 24). Compared to La(CrFeCoNiCu)O_3, the OH^- peak of La(CrFeCoNiCu)O_3–OH shifted by approximately 0.7 eV toward lower binding energy, indicating in-situ hydroxylation induced interface electron enrichment[45]. Taken together, in-situ ATR-SEIRAS measurements align with theoretical predictions, demonstrating that La(CrFeCoNiCu)O_3 can in-situ hydroxylation to enhance uranium capture.

We further investigated the specific processes of hydroxylation through soft X-ray absorption structure (XAS), quasi-in-situ XPS, and DFT calculations. For O K-edge XAS spectra, the pre-edge peak can be attributed to the excitation of O 1*s* electrons into hybrid orbitals formed by O 2*p* and transition metal M 3*d* orbitals (O 2*p*-M 3*d*)[46]. The intensity order of the pre-edge peak is: $LaCrO_3$ > La(CrFeCoNiCu)O_3 > La(CrFeCoNiCu)O_3–OH. Compared with $LaCrO_3$, the pre-edge peak intensity of La(CrFeCoNiCu)O_3 exhibited marked attenuation, indicating that the introduction of multiple elements significantly weaken metal-oxygen covalency (Fig. 4c)[47]. The above results corroborated prior experimental finding that $LaCrO_3$ is not prone to surface hydroxylation in electro-assisted uranium extraction reactions. For La(CrFeCoNiCu)O_3–OH, the further attenuated pre-edge peak intensity is attributed to the downward shift of electron density around oxygen induced by hydrogen in hydroxyl groups, resulting in further attenuation of metal-oxygen covalency[48,49]. Meanwhile, Cu 2*p* XPS further validated the above conclusion. Compared with La(CrFeCoNiCu)O_3 before reaction, the Cu^{2+} $2p_{1/2}$ peak at 956.5 eV and the Cu^{2+} $2p_{3/2}$ peak at 936.2 eV gradually shifted towards lower binding energies, with the peak areas diminishing until completely disappearance. Meawhile, the area of Cu^{1+} $2p_{1/2}$ peak at 952.7 eV and the Cu^{1+} $2p_{3/2}$ peak at 932.7 eV gradually increased, which is consistent with the Cu^{2+} 2*p* peaks evolution, further confirming the reconstruction of Cu sites (Fig. 4d)[50]. In contrast, as structural stabilizers, La and Ni did not show significant changes during the reaction. For the XPS spectra of Cr, Co, and Fe, only slight changes were observed, which may be attributed to their partial leaching or rearrangement (Supplementary Fig. 25)[51]. Cu *L*-edge XAS spectrum of La(CrFeCoNiCu)O_3 revealed that the intensity of the L_3 edge of La(CrFeCoNiCu)O_3-OH remained basically unchanged versus the pristine sample, while the intensity of the L_2 edge increased and slightly shifted negatively. (Supplementary Fig. 26), indicating that reduced *d*-orbital electron occupancy from coordination restructuring[47,52]. Collectively, these results identify Cu as the hydroxylation sites in La(CrFeCoNiCu)O_3.

The electron redistribution in La(CrFeCoNiCu)O_3 was revealed through DCD diagram and Bader charge analysis. As shown in Fig. 4e, the Bader charge value for the Cu atom was merely 0.59 $|e^-|$, accompanied by extensive yellow regions surrounding it. This indicats significant electron accumulation around the Cu atom, enhancing its reactivity and rendering it more susceptible to hydroxylation during the reaction. Notably, the Bader charge value of Cr was substantially higher at 1.86 $|e^-|$, surrounded by considerable electron depletion regions. Such uneven electron distribution can be explained by the high-entropy effect[53]. As shown in Supplementary Fig. 27, the electronic state height of Cr in $LaCrO_3$ was localized near the Fermi level (E_f), presenting a sharp single peak with a *d*-band center of -0.567 eV. For La(CrFeCoNiCu)O_3, elements with stronger electronegativity such as Cu intercept electrons through the oxygen ligand network to redistribute electrons[52]. This result leads to downward shift the *d*-band center of Cr (-1.777 eV), presenting a broadened double peak. The total density of states (TDOS) analysis demonstrated that La(CrFeCoNiCu)O_3 exhibited significantly enhanced electron density near the E_f compared to $LaCrO_3$, indicating pronounced alterations in its electronic structure (Supplementary Fig. 28). Projected density of states (PDOS) analysis revealed that the orbital overlap region between Cu and O was substantially larger than that of other metals, signifying a strong interaction between Cu and O and confirming electron redistribution within La(CrFeCoNiCu)O_3 (Fig. 4f). Following hydroxylation, the overlap region between the Cu and O densities of states noticeably decreased, while the *d*/*p* band center differences ($\Delta\varepsilon_{d-p}$) significantly increased (|0.179| eV vs. |2.032| eV). This indicated weakened orbital hybridization and diminished electronic coupling between Cu and O, consistent with the findings from O *K*-edge XAS spectra (Fig. 4g and 4h)[54]. This can be attributed to the directional migration of electrons along the Cu-O-H structure towards the O atom

in the hydroxyl group, with subsequent accumulation near the H atom. These findings illustrated the high-entropy effect in modulating electronic properties of La(CrFeCoNiCu)O_3 and provided key evidence for Cu sites as centers of in-situ hydroxylation. Based on the above analysis, we have summarized the in-situ hydroxylation processes of La(CrFeCoNiCu)O_3 and the reaction pathway of $UO_2F_X^{\pm n}$ species at hydroxylated sites (Fig. 4i). The entire reaction processes can be roughly divided into the following steps. Firstly, under the drive of an electric field, in-situ hydroxylation reactions occurred at the Cu sites due to the charge differences of each element in La(CrFeCoNiCu)O_3. The formed Cu-O-H active sites served as an effective sites for confining and capturing free uranyl species, which are subsequently reduced by electrons accumulated near these sites. Finally, with the assistance of alkali metal (K^+) in the solution medium, further crystallization and mineralization are carried out to form $K_2UO_2F_5$ mineral[3,4].

3.5. Verifying in real nuclear wastewater

Motivated by the exceptional extraction performance of La(CrFeCoNiCu)O_3 in simulated nuclear wastewater, we further validated its efficacy in more complex real nuclear wastewater systems. Consequently, we conducted further experiments using a self-assembly setup with triple tandem electrolytic cell. This apparatus primarily consists of four components: a power supply system, a tandem electrolytic cell, a circulation system, and an automated control system (Fig. 5a). The detailed composition of the real nuclear wastewater is presented in the inset of Fig. 5b inset. Prior to large-scale treatment of real nuclear wastewater, we first verified the superiority of La(CrFeCoNiCu)O_3 using 50 mL of real nuclear wastewater. The results demonstrated that, yellow uranium products were enriched on the electrode sheets after 6 h of extraction, achieving an extraction efficiency of 91.4%, which was significantly higher than those of La(CrCoNi)O_3 and $LaCrO_3$ (Fig. 5b).

Meanwhile, the collected mineralized uranium precipitate (abbreviated as MUP) was further tested using X-ray absorption fine structure (XAFS) measurements, XRD, and XPS to confirm the valence state and crystal structure of the uranium species. As shown in Fig. 5c, the absorption edge position of the MUP is close to that of U_3O_8 and lies between those of UO_2 and $UO_2(NO_3)_2$. This indicates that the valence state of MUP ranges between + 4 and + 6, which is consistent with the U 5*f* XPS analysis results (Supplementary Fig. 29), suggesting an electrochemical reduction process. The Fourier-transform (FT) k^2-weighted extended X-ray absorption fine structure (EXAFS) spectra of the MUP exhibited two distinct main peaks at 1.3 Å and 2.2 Å, which are significantly different from the standard sample (Supplementary Fig. 30). Furthermore, wavelet measurements (WT) of the MUP further demonstrate their significant differences from the standard sample, which strongly confirms the structural transformation of uranium during the electrochemical reduction process (Fig. 5d). Finally, the phase structure was further analyzed by XRD pattern, confirming that the MUP is $K_2U_2O_7$ in a mixed valence state (Fig. 5e). This is significantly different from the uranium products obtained in simulated nuclear wastewater, further confirming the complexity of real wastewater. The above results indicates that La(CrFeCoNiCu)O_3 can maintain excellent performance even in complex environments of real nuclear wastewater.

Subsequently, we further began the industrial scale performance evaluation of real nuclear wastewater. The three electrode sheets (each loaded with 400 mg of materials) were connected in parallel within the triple tandem electrolytic cell to treat 2.5 L of real nuclear wastewater (10 V, 1 A). As shown in Fig. 5f, the uranium concentration decreased from an initial 514 mg L^{-1} to ~ 9.5 mg L^{-1} after 8 h of reaction, and the nuclear wastewater transitioned from its original yellow color to a colorless transparent liquid. Substantial solid deposits were observed on both the electrode sheets and the bottom of the electrolytic cell, yielding approximately 1.3 g of collected product (Supplementary Fig. 31). This work preliminarily confirmed recovery of uranium from fluoride-containing uranium wastewater through electrochemical methods, achieving secondary recovery and reuse of uranium resources (Fig. 5g). To better illustrate the promoting effect of this work on uranium cycle regeneration, we estimated the power consumption throughout the extraction processes. The total electricity consumption was calculated as 80 W·h, corresponding to 73.03 kW·h ($5.33) required to extract 1 kg of U_3O_8. Factoring in costs associated with chemicals ($3), materials synthesis ($2), electrode fabrication ($2), and post-processing of uranium products ($3.5), the total expenditure for extracting 1 kg of uranium product (U_3O_8) is approximately $15.83 (Fig. 5h). Additionally, the cost of producing 1 kg uranium from real nuclear wastewater through our method is much lower than the international market price of natural uranium[55] and the cost of recovering uranium from wastewater through adsorption method (Fig. 5i)[56]. Therefore, this work demonstrated the potential of La(CrFeCoNiCu)O_3 as a promising electrode candidate for large-scale treatment of real nuclear wastewater, while also confirming its economic feasibility.

4. Conclusion

In summary, we report an in-situ surface hydroxylation strategy induced by high entropy effect for the recovery of uranium from fluoride containing uranium wastewater. Guided by DFT calculations, a La(CrFeCoNiCu)O_3 high-entropy oxide was synthesized via a modified sol-gel method. Relying on soft XAS, along with DFT calculations, we have confirmed that the electron accumulation at Cu sites promotes in-situ dynamic surface hydroxylation driven by high entropy effect, thus forming electron enriched M-OH active sites. As expected, La(CrFeCoNiCu)O_3 achieved an adsorption capacity of 2385.8 mg g^{-1} with uranium extraction efficiency up to 97.8% in simulated nuclear wastewater containing 30 g L^{-1} fluoride. In addition, we have independently developed a flow electrochemical device to evaluate the

continuous treatment capacity of real nuclear wastewater on an industrial scale. For 2.5L of real nuclear wastewater, La(CrFeCoNiCu)O_3 achieved an extraction efficiency of 98.1% within 8 h, while recovering 1.3 g of uranium product. This study not only developed a high-performance electrode materials suitable for uranium recovery from high-fluoride wastewater but also provided novel insights into the design of dynamic active sites on electrode surfaces.

Declarations

Acknowledgments

This work was supported by NSFC (U2267224, W.Z.). The Project of State Key Laboratory of Environment-Friendly Energy Materials in SWUST (No.20fksy19, W.Z.). Doctoral Fund of Southwest University of Science and Technology (No.23zx7103, T.C.). The authors express their gratitude to the Theoretical and Computational Chemistry Team at Shiyanjia Lab (www.shiyanjia.com) for their invaluable assistance. Additionally, the authors acknowledge Shiyanjia Lab (www.shiyanjia.com) for providing invaluable support with SEM, TEM, and XPS analysis.

References

1. Chen T, Yu K, Dong C, Yuan X, Gong X, Lian J, Cao X, Li M, Zhou L, Hu B, He R, Zhu W, Wang X (2022) Advanced Photocatalysts for Uranium Extraction: Elaborate Design and Future Perspectives. Coord Chem Rev 467:214615
2. Wang Y, Wen G, Liu Z, Thuy Nga TT, Dong C-L, You J, Xie C, Du S, Zhang F, Liu Q, Wei J, Cao Y, Peng X, Yuan Y, Wang Y, Wang S (2025) Bipolar Electrochemical Uranium Extraction from Seawater with Ultra-Low Cell Voltage. Nat Sustain 8(6):682–691
3. Li G, Liu Y, Jiao C, Jiang Z, Zhang J, Chen T, Lin T, He R, Zhu W, Wang X (2025) Direct Recovery of High-Purity Uranium from Fluoride-Containing Nuclear Wastewater via Extraction Materials with Ensemble Lewis Sites and a Tandem Electrochemical Device. Water Res 279:123467
4. Lin T, Chen T, Jiao C, Zhang H, Hou K, Jin H, Liu Y, Zhu W, He R (2024) Ion Pair Sites for Efficient Electrochemical Extraction of Uranium in Real Nuclear Wastewater. Nat Commun 15(1):4149
5. Li J, Hu Y, Shen Z, Jin H, He R, Zhu W, Zhao G, Ji Z, Ma B, Wang X (2025) Efficient Uranium (VI) Recovery from Fluorinated Wastewater via Deferiprone Ligand Complexation. Water Res 271:122884
6. Zhang QY, Zhang LJ, Zhu JQ, Gong LL, Huang ZC, Gao F, Wang JQ, Xie XQ, Luo F (2024) Ultra-Selective Uranium Separation by in-Situ Formation of π-f Conjugated 2D Uranium-Organic Framework. Nat Commun 15(1):453
7. Wei J, Chen S, Jiang Y, Liu Z, Wang Y, You J, Zhang F, Cao Y, Wang S, Wang Y (2023) Selective Anchoring by Surface Sulfur Species Coupled with Rapid Interface Electron Transfer for Ultrahigh Capacity Extraction of Uranium from Seawater. Environ Sci Technol 57(51):21908–21916
8. Chen S, Wang X, Zheng H, Wang Z, Wang X, Lin Z, Feng S, Zhang C, Sun T, Zhu J (2025) Electron-Buffering Rechargeable Microelectrode Adsorbents for Rapid Environmental Remediation of Uranium-Containing Wastewater. Nat Water 3(8):937–948
9. Guo L, Liu Y, Jia Y, Huang ZC, Gong L, Xie X, Luo F (2025) Control on the Stacking Mode in a Sulfonic Covalent Organic Framework Enabling a Precise Uranyl-Identified Pocket for Ultrahigh-Capacity Uranium Extraction from Seawater. J Am Chem Soc 147(34):31340–31348
10. Wang X, Hu H, Liu J, Hu J, Han C, Attfield JP, Yang M (2025) Anion-Exchange Membrane Electrolysis for Efficient Uranium Extraction from Saline Wastewater. Adv Mater e08705
11. Wang Y, Xie C, Wang G, Zhang F, Xiao Z, Wang J, Wang Y, Wang S (2024) Electrochemistry-Assisted in-Situ Regeneration of Oxygen Vacancies and Ti(III) Active Sites for Persistent Uranium Recovery at a Low Potential. Water Res 258:121817
12. Hu J, Guo T, Zhong X, Li J, Mei Y, Zhang C, Feng Y, Sun M, Meng L, Wang Z, Huang B, Zhang L, Wang Z (2024) Situ Reconstruction of High-Entropy Heterostructure Catalysts for Stable Oxygen Evolution Electrocatalysis under Industrial Conditions. Adv Mater 36(14):2310918
13. Deng X, Kusada K, Yamamoto T, Toriyama T, Murakami Y, Tseng J, Yamada H, Sakata O, Ashitani H, Kawaguchi S, Kubota Y, Kitagawa H (2025) Platinum-Group Metal High-Entropy Selenides for the Hydrogen Evolution Reaction. Angew Chem Int Ed 64(2):e202414786
14. Jiang P, Xu Y, Gong Z, Ge B, Ding L, Huang C, Qiu X, Pei Z (2025) Entropy-Driven Competitive Adsorption Sites Tailoring Unlocks Efficient Hybrid Conversion Zn–Air Batteries. Angew Chem Int Ed. 64 (24), e202504188
15. Kresse G, Furthmüller J (1996) Efficient Iterative Schemes for *Ab Initio* Total-Energy Calculations Using a Plane-Wave Basis Set. Phys Rev B 54(16):11169
16. Blöchl PE (1994) Projector Augmented-Wave Method. Phys Rev B 50(24):17953–17979
17. Perdew JP, Burke K, Ernzerhof M (1996) Generalized Gradient Approximation Made Simple. Phys Rev Lett 77(18):3865–3868

18. Grimme S, Semiempirical (2006) GGA-type Density Functional Constructed with a Long-range Dispersion Correction. J Comput Chem 27(15):1787–1799
19. Wu H, Lu Q, Li Y, Zhao M, Wang J, Li Y, Zhang J, Zheng X, Han X, Zhao N, Li J, Liu Y, Deng Y, Hu W (2023) Structural Framework-Guided Universal Design of High-Entropy Compounds for Efficient Energy Catalysis. J Am Chem Soc 145(3):1924–1935
20. Yao Z, Chen Y, Wang X, Hu K, Ren S, Zhang J, Song Z, Ren N, Duan X (2025) High-Entropy Alloys Catalyzing Polymeric Transformation of Water Pollutants with Remarkably Improved Electron Utilization Efficiency. Nat Commun 16(1):148
21. Liao M, Wang C, Chen Y, Chen Y, Qin C, Li Y (2025) Self-Reconstruction Mechanism of High-Entropy Oxide in Glycerol Steam Reforming: The Key to H_2 -Rich Syngas Production. ACS Catal 15(6):4845–4857
22. Hu W, Yang L, Shao P, Shi H, Chang Z, Fang D, Wei Y, Feng Y, Huang Y, Yu K, Luo X (2022) Proton Self-Enhanced Hydroxyl-Enriched Cerium Oxide for Effective Arsenic Extraction from Strongly Acidic Wastewater. Environ Sci Technol 56(14):10412–10422
23. Zhang H, Li J, Liu J, Gao Y, Fan Y, Liu X, Guo C, Liu H, Chen X, Wu X, Liu Y, Gu Q, Li L, Wang J, Chou S-L (2025) Understanding Capacity Fading from Structural Degradation in Prussian Blue Analogues for Wide-Temperature Sodium-Ion Cylindrical Battery. Nat Commun 16(1):2520
24. Qi S, Lei Z, Huo Q, Zhao J, Huang T, Meng N, Liao J, Yi J, Shang C, Zhang X, Yang H, Hu Q, He C (2024) Ultrathin High-Entropy Fe-Based Spinel Oxide Nanosheets with Metalloid Band Structures for Efficient Nitrate Reduction toward Ammonia. Adv Mater 36(27):2403958
25. Aamlid SS, Oudah M, Rottler J, Hallas AM (2023) Understanding the Role of Entropy in High Entropy Oxides. J Am Chem Soc 145(11):5991–6006
26. Wang Q, Liu X, He D, Wang DF, Comprehension (2023) Synthetic Procedures and Catalytic Applications of High Entropy Oxide Nanomaterials. Mater Today 70:218–236
27. Sun H, Song J, Shi P, Cheng Z, Tian L, Zhou M, Qi T (2024) Selective Detection of NO Using the Perovskite-Type Oxide $LaMO_3$ (M = Cr, Mn, Fe, Co, and Ni) as the Electrode Material for Yttrium-Stabilized Zirconia-Based Electrochemical Sensors. J Mater Chem A 12(29):18234–18247
28. Zhang J, Yu Z, Zhu Y, Cai J, Wang M, Gao P, Zhang Y, Zhang N, Wang D, Shen Y, Wang M (2025) Configuration Design and Interface Reconstruction to Realize the Superior High-Rate Performance for Sodium Layered Oxide Cathodes. Adv Energy Mater 15(23):2405951
29. Liu L, Zhang S, Ma Z, Zhu S (2020) Effects of Ca2+-Sr2 + Doping on the Infrared Emissivity of LaCrO3. Ceram Int 46(12):19738–19742
30. Zhao T, Zhao J, Tao X, Yu H, Li M, Zeng J, Wang H (2022) Highly Active and Thermostable Submonolayer La(NiCo)OΔ Catalyst Stabilized by a Perovskite $LaCrO_3$ Support. Commun Chem 5(1):70
31. Yin P, Niu X, Li S-B, Chen K, Zhang X, Zuo M, Zhang L, Liang H-W (2024) Machine-Learning-Accelerated Design of High-Performance Platinum Intermetallic Nanoparticle Fuel Cell Catalysts. Nat Commun 15(1):415
32. Ren L, Zhang K, Huang Y-C, Lu YR, Deng H, Ding Y, Chen C, Huang B, Hua W, Fu L, Zhao X, Shen S, Wei J, Chen J (2025) Tailored Interatomic Interactions in High-Entropy Alloys for Enhanced Electrocatalytic Hydrogen Evolution Reaction in Alkaline Water. ACS Catal 15(13):11022–11033
33. Zhou S, Liao J, Zhang W, Dai P, Yu C, Gao T, Hou T, Cao G, Zhao S (2025) High-Entropy Li-Rich Layered Cathodes with Negligible Voltage Decay through Migration Retardation Effect. Adv Mater 37(32):2505189
34. Wang X, Li G, Huang H, Jin H, Liu Y, Yang F, He R, Zhu W (2025) Implanting Open Active Pairs into Open Flower-Structured Cu-S-O Nanosheets for Electrochemical Uranium Extraction in Radioactive Wastewater. Appl Catal B: Environ Energy 367:125081
35. Wang R, Li M, Liu T, Li X, Zhou L, Tang L, Gong C, Gong X, Yu K, Li N, Zhu W, Chen T (2022) Encapsulating Carbon-Coated Nano Zero-Valent Iron Particles with Biomass-Derived Carbon Aerogel for Efficient Uranium Extraction from Uranium-Containing Wastewater. J Clean Prod 364:132654
36. Zhang F, Dong H, Li Y, Fu D, Yang L, Shang Y, Li Q, Shao Y, Gang W, Ding T, Chen T, Zhu W (2024) In Situ Metal-Oxygen-Hydrogen Modified B-TiO_2 @Co_2P-X S-Scheme Heterojunction Effectively Enhanced Charge Separation for Photo-assisted Uranium Reduction. Adv Sci 11(5):2305439
37. Tu B, Yu K, Fu D, Zhou L, Wang R, Jiang X, Liu H, Cao X, Gong X, He R, Tang Y, Chen T, Zhu W (2023) Amino-Rich Ag-NWs/NH_2-MIL-125(Ti) Hybrid Heterostructure via LSPR Effect for Photo-Assist Uranium Extraction from Fluorine-Containing Uranium Wastewater without Sacrificial Agents. Appl Catal B 337:122965
38. Zhou L, Lian J, Li Q, Li J, Shao Y, Wu G, Ding T, Cui X, Chen T, Zhu W (2023) Unveiling the Critical Role of Surface Hydroxyl Groups for Electro-Assisted Uranium Extraction from Wastewater. Inorg Chem 62(51):21518–21527
39. Zhou Y, Yang J, Zhou N, Hao H, Jiang X, Lei F, Shi K, Zhao Y, Zhou G, Liu T, Xing S (2023) Amidoxime-Functionalized MXene Beads for the Effective Capture of Uranium from Wastewater with High Fluoride Concentrations. Chem Eng J 471:144647

40. Yang S, Yan C, Huang B, Jin T, Guo D, Xiao M, Qian Y (2025) PBTCA-Modified Self-Crosslinked Chitosan Gels for Efficient Electrosorption of Uranium from Wastewater. Desalination 612:118984
41. Yan Z, Tao S, Wang J, Lu X, Lu T (2024) Unlocking Efficient Alkaline Hydrogen Evolution Through Ru–Sn Dual Metal Sites and a Novel Hydroxyl Spillover Effect. Adv Mater 36(46):2411942
42. Feng H, Dong H, He P, He J, Hu E, Qian Z, Li J, Li J, Zhu W, Chen T (2024) Nickel Single Atom Mediated Phosphate Functionalization of Moss Derived Biochar Effectively Enhances Electrochemical Uranium Extraction from Seawater. J Mater Chem A 12(13):7896–7905
43. Yu K, Tang L, Cao X, Guo Z, Zhang Y, Li N, Dong C, Gong X, Chen T, He R, Zhu W (2022) Semiconducting Metal–Organic Frameworks Decorated with Spatially Separated Dual Cocatalysts for Efficient Uranium (VI) Photoreduction. Adv Funct Mater 32(20):2200315
44. Zhou M, Andrews L, Ismail N, Marsden C (2000) Infrared Spectra of UO_2, UO_2^+, and UO_2^- in Solid Neon. J Phys Chem A 104(23):5495–5502
45. Tang Y, Wu C, Zhang Q, Zhong H, Zou A, Li J, Ma Y, An H, Yu Z, Xi S, Xue J, Wang X, Wu J (2023) Accelerated Surface Reconstruction through Regulating the Solid-Liquid Interface by Oxyanions in Perovskite Electrocatalysts for Enhanced Oxygen Evolution. Angew Chem Int Ed. 62 (37), e202309107
46. Tang B, Zhou Y, Ji Q, Zhuang Z, Zhang L, Wang C, Hu H, Wang H, Mei B, Song F, Yang S, Weckhuysen BM, Tan H, Wang D, Yan WA (2024) Janus Dual-Atom Catalyst for Electrocatalytic Oxygen Reduction and Evolution. Nat Synth 3(7):878–890
47. Hooch Antink W, Lee S, Lee HS, Shin H, Yoo TY, Ko W, Shim J, Na G, Sung Y, Hyeon T (2024) High-Valence Metal-Driven Electronic Modulation for Boosting Oxygen Evolution Reaction in High-Entropy Spinel Oxide. Adv Funct Mater 34(1):2309438
48. Wang M, Li X, Wang Z, Huang H, Sun X, Chen H, Luo H, Li L, Zou X, Zhao X (2025) Nonmetal–Metal Strategy to Reduce Ru–O Covalency While Promoting Local Reactive Water Concentration for Efficient Acidic Oxygen Evolution. Nano Lett 25(31):12009–12018
49. Hou X, Ni T, Zhang Z, Zhou J, Zhang S, Chu L, Dai S, Wang H, Huang M (2024) Reinforcing Built-in Electric Field via Weakening Metal–Oxygen Covalency within MOFs-Based Heterointerface for Robust Oxygen Evolution Reaction. Chem Eng J 495:153464
50. Chen X, Jia S, Zhai J, Jiao J, Dong M, Xue C, Deng T, Cheng H, Xia Z, Chen C, Xing X, Zeng J, Wu H, He M, Han B (2024) Multivalent Cu Sites Synergistically Adjust Carbonaceous Intermediates Adsorption for Electrocatalytic Ethanol Production. Nat Commun 15(1):7691
51. Huang Y, Wang Z, Xiao H, Liu Q, Wang X (2024) Activating and Stabilizing Lattice Oxygen via Self-Adaptive Zn–NiOOH Sub-Nanowires for Oxygen Evolution Reaction. J Am Chem Soc 146(42):29006–29016
52. Chen C, Wang Y-R, Wang Y-J, Zhou J-H, Li Y-Q, Shen P-X, Guo Z-Y, Li W-W (2025) Built-In Electric Field Augments Hypersalinity Resistance of Heterostructured Metal Oxides for Efficient Fenton-like Catalysis. ACS Nano 19(32):29616–29626
53. Sun N, Zheng Z, Lai Z, Wang J, Du P, Ying T, Wang H, Xu J, Yu R, Hu Z, Pao C, Huang W, Bi K, Lei M, Huang K (2024) Augmented Electrochemical Oxygen Evolution by d–p Orbital Electron Coupling. Adv Mater. 2404772
54. Feng K, Wang H, Zhou S, Zhang W, Gong C, He Y, Wang Y, Dai W, Li J, Zhang Z, Li S (2025) Surface Engineering-Induced d-Band Center Down-Regulation in High-Entropy Alloy Nanowires for Enhanced Nanozyme Catalysis. Adv Sci 12(25):2502354
55. Pedregal DJ (2020) Forecasting Uranium Prices: Some Empirical Results. Nuclear Eng Technol 52(6):1334–1339
56. Liu Y, Ni S, Wang W, Zhao Y, Meng Y, Liu H, Yang L (2024) Facile and Scalable Synthesis of Functionalized Hierarchical Porous Polymers for Efficient Uranium Adsorption. Water Res 257:121683

Tables

Tables are available in the Supplementary Files section.

Figures

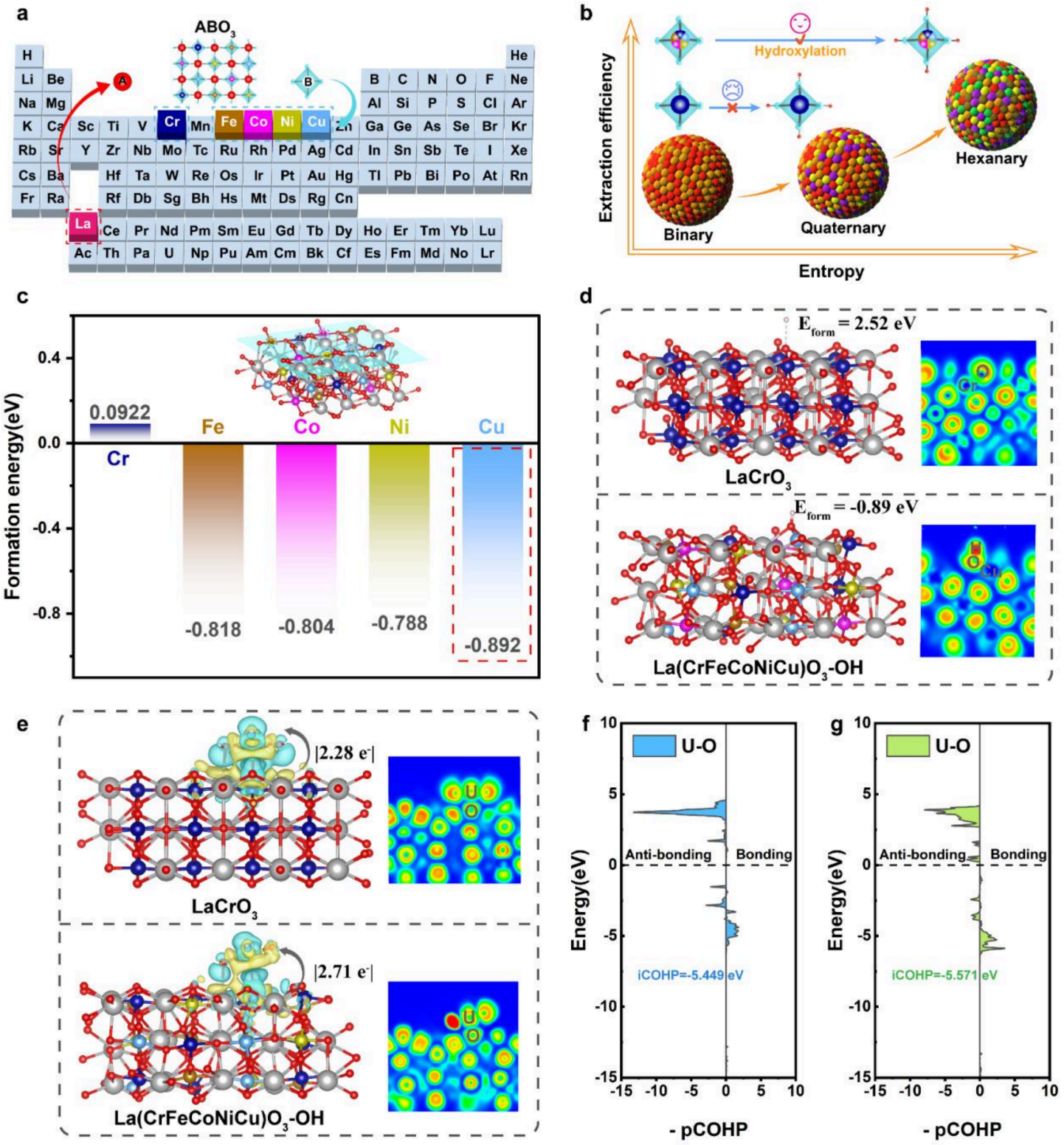


Figure 1

(a) Elemental design of high entropy perovskite. (b) Entropy-driven hydroxylation strategy. (c) The formation energy of hydroxyl at different sites on the surface of La(CrFeCoNiCu)O_3. (d) The hydroxyl formation energy and corresponding ELF mapping of $LaCrO_3$ and La(CrFeCoNiCu)O_3. (e) Bader charge analysis, differential charge density and ELF mapping of UO_2F^+ adsorption on $LaCrO_3$ and La(CrFeCoNiCu)O_3-OH (yellow represents electron accumulation, cyan represents electron dissipation). (f)COHP curves of UO_2F^+ on $LaCrO_3$ (f) and La(CrFeCoNiCu)O_3-OH (g).

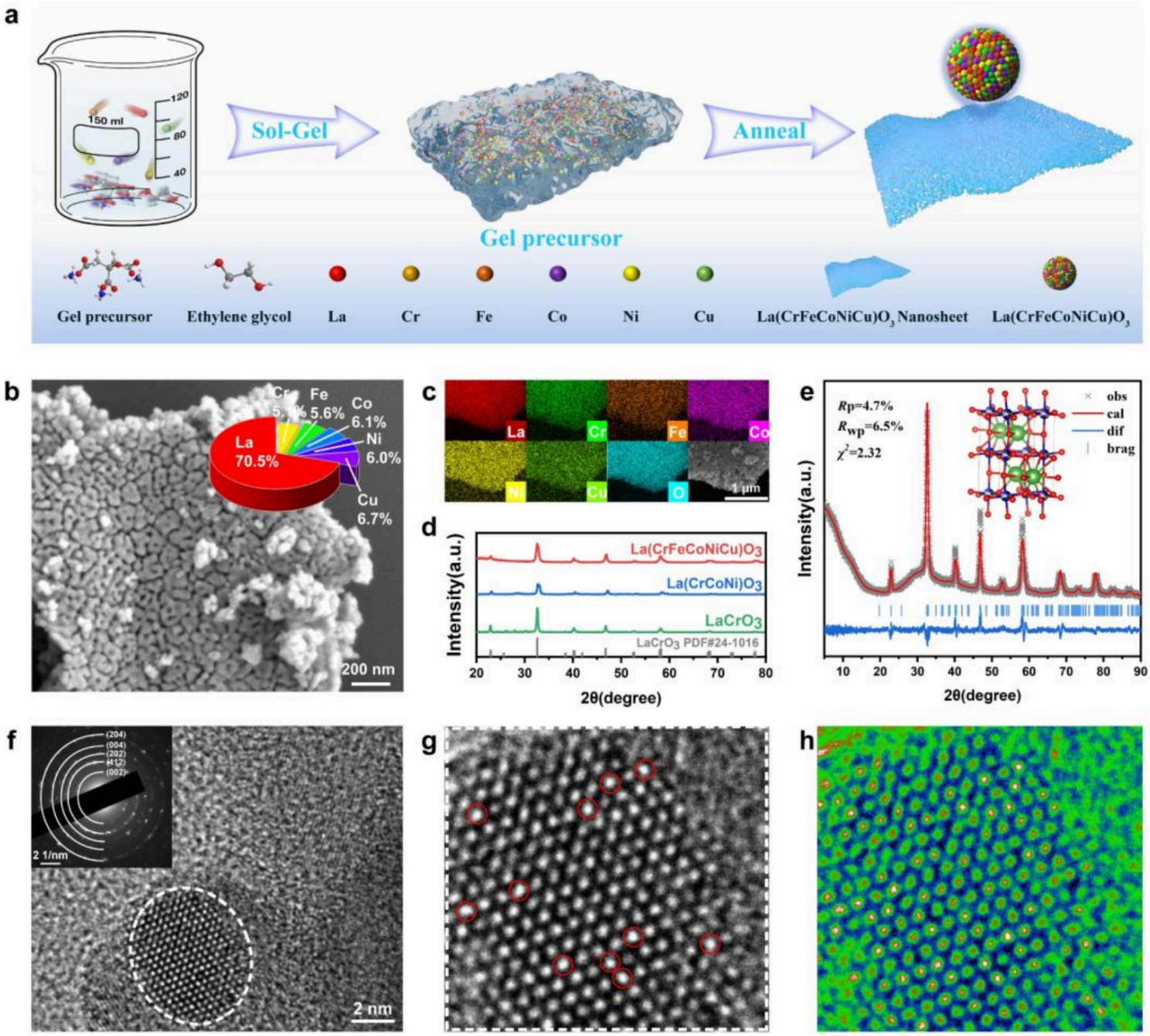


Figure 2

(a) Schematic diagram of the synthesis for La(CrFeCoNiCu)O_3. (b) SEM image of La(CrFeCoNiCu)O_3 (inset: elemental composition determined by ICP-MS). (c) EDS elemental mapping images of La(CrFeCoNiCu)O_3. (d) XRD patterns of La(CrFeCoNiCu)O_3, La(CrCoNi)O_3 and $LaCrO_3$. (e) Rietveld refinement plot for the XRD pattern of La(CrFeCoNiCu)O_3. (f) HADDF-STEM image of La(CrFeCoNiCu)O_3 (inset: corresponding SAED pattern). (g) Magnified region in (f), and La atoms are highlighted by red circles). (h) Magnified region from(f) under polarized imaging mode.

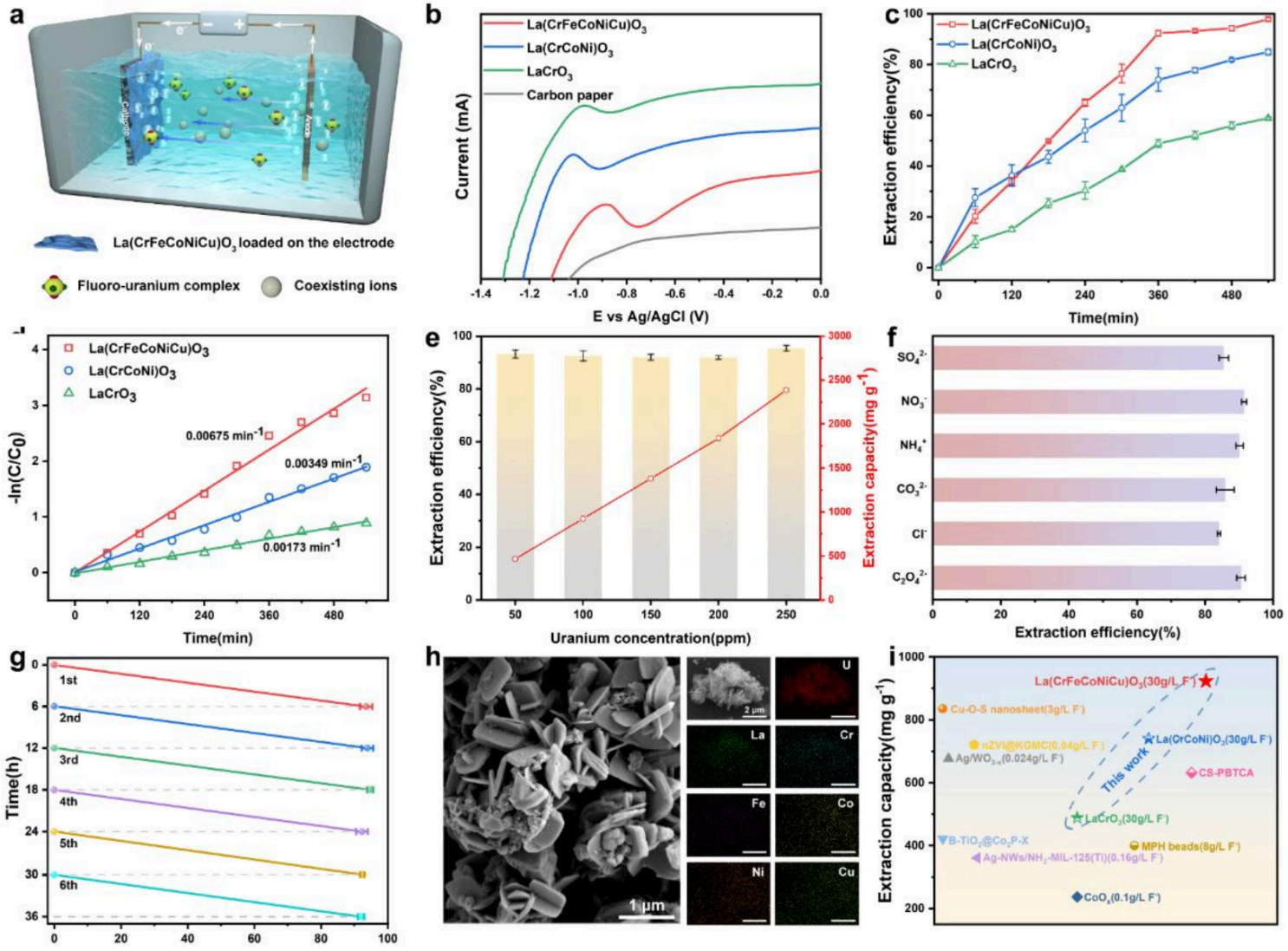


Figure 3

(a) Schematic diagram of uranium extraction experiment. (b) LSV curves of $La(CrFeCoNiCu)O_3$, $La(CrCoNi)O_3$, and $LaCrO_3$. (c) Extraction efficiency of uranium and (d) corresponding kinetic constants for $La(CrFeCoNiCu)O_3$, $La(CrCoNi)O_3$, and $LaCrO_3$. (e) Uranium extraction efficiency and extraction capacity of $La(CrFeCoNiCu)O_3$ under different initial uranium concentrations. (f) Extraction efficiency of uranium in the presence of competitive ions (competing ions concentration: 1 g L^{-1}). (g) Reusability of $La(CrFeCoNiCu)O_3$. (h) SEM image of $La(CrFeCoNiCu)O_3$ after uranium extraction. (i) Uranium extraction capacity compared to reported materials.

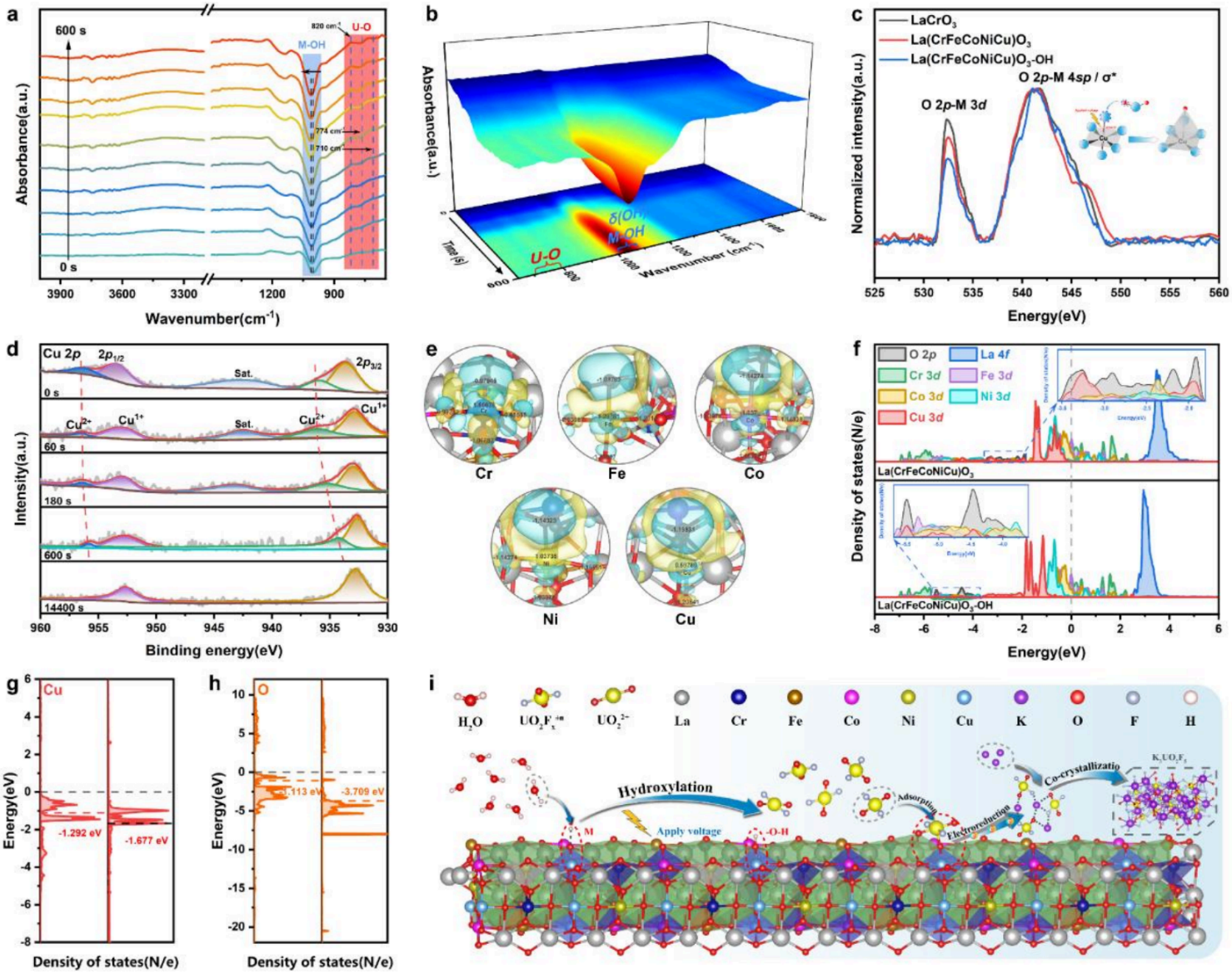


Figure 4

(a) The in-situ ATR-SEIRAS of La(CrFeCoNiCu)O_3 (experimental condition: 250 mg L^{-1} U(Ⅵ), 30 g L^{-1} F, -1.7 V). (b) 3D mapping of in-situ ATR-SEIRAS for La(CrFeCoNiCu)O_3. (c)The O XAS spectra of $LaCrO_3$, La(CrFeCoNiCu)O_3 and La(CrFeCoNiCu)O_3-H. (d) XPS spectra of Cu in La(CrFeCoNiCu)O_3 at different time. (e) Bader charge analysis and differential charge density distribution of La(CrFeCoNiCu)O_3 (yellow represents electron accumulation, cyan represents electron dissipation). (f) The PDOS of La(CrFeCoNiCu)O_3 and La(CrFeCoNiCu)O_3-OH. The transformation of *d*-band center (g) and p-band center (h) after hydroxylation of La(CrFeCoNiCu)O_3. (i) The mechanism diagram of in-situ hydroxylation and uranyl capture of La(CrFeCoNiCu)O_3.

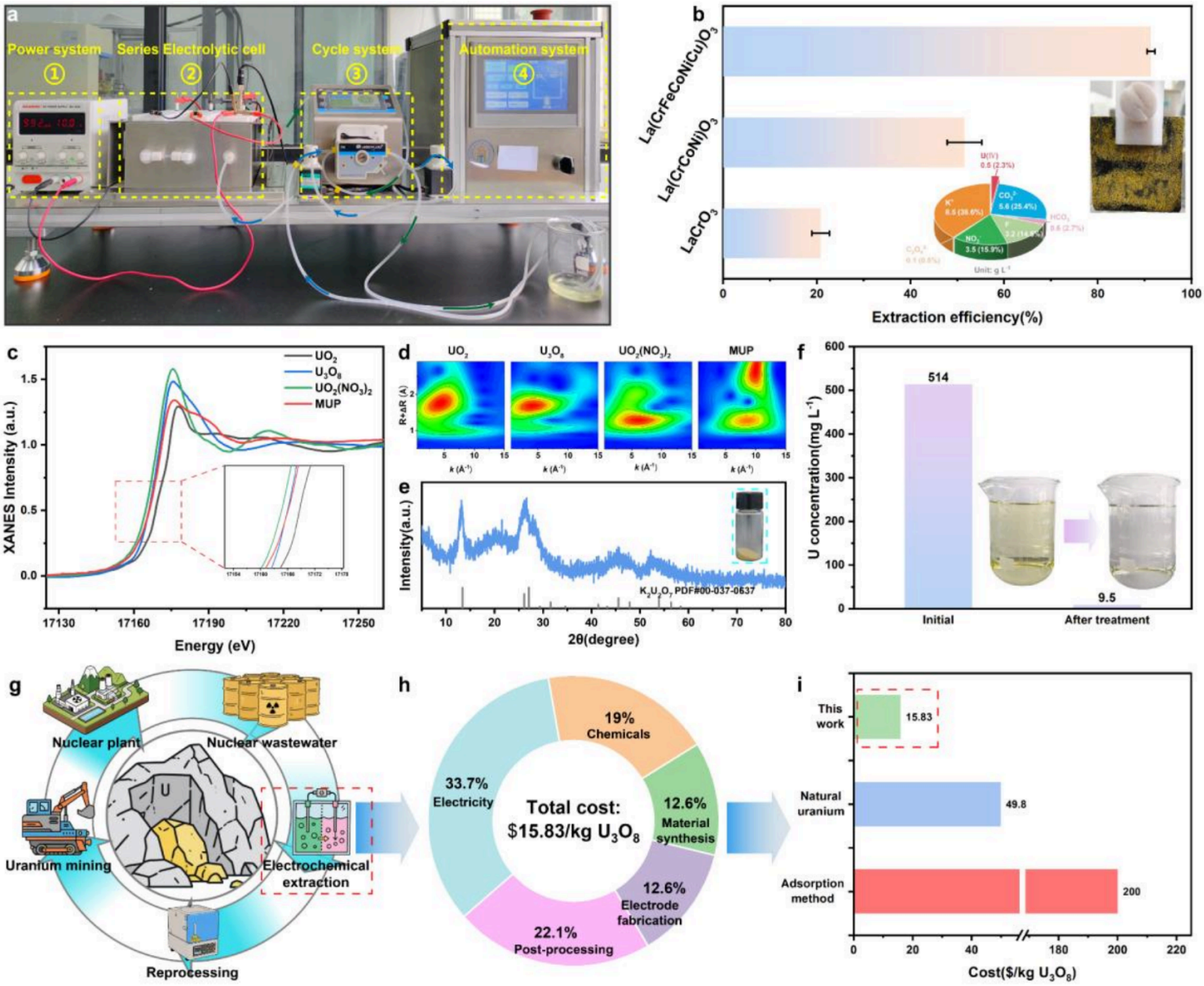


Figure 5

(a) Self-assembly setup with triple tandem electrolytic cell (blue and green represent inlet and outlet, respectively). (b) Extraction efficiency of $La(CrFeCoNiCu)O_3$, $La(CrCoNi)O_3$, and $LaCrO_3$ in real nuclear wastewater. (c) The U L_3-edge XANES (inset: magnified pre-edge XANES region) and (d) wavelet analysis of UO_2, U_3O_8, $UO_2(NO_3)_2$ and the mineralized uranium precipitate (abbreviated as MUP). (e) XRD pattern of the MUP (inset: digital photograph of the MUP). (f) Variation in uranium concentration after 8 h of extraction (using 2.5 L of real nuclear wastewater). (g) The cycle of uranium in nuclear fuel. (h) The cost proportion of uranium regeneration in this work. (i) Comparison of cost between this work and natural uranium and adsorption methods.

Supplementary Files

This is a list of supplementary files associated with this preprint. Click to download.

- SIHighEntropyEffectInducedInsituSurfaceHydroxylationforRobustElectroAssistedUraniumMineralizationfromRealNuclearWastewater.docx
- Tables.docx